

## Non-Adiabatic Direct Dynamics Study of Chromium Hexacarbonyl Photodissociation

Martin J. Paterson, Patricia A. Hunt, and Michael A. Robb\*

Department of Chemistry, Kings College, London, Strand, WC2R 2LS, United Kingdom

Ohgi Takahashi

Department of Chemistry, University of Tsukuba, Tsukuba 305-8571, Japan

Received: June 27, 2002; In Final Form: August 15, 2002

The photodissociation of  $\text{Cr}(\text{CO})_6$  has been studied using direct dynamics including trajectory surface hopping. The dissociation takes place on a steep excited-state potential surface leading to ejection of a CO ligand within 100 fs in reasonable agreement with time-resolved studies by Fuß et al.<sup>1–3</sup> Our dynamics studies of the  $\text{Cr}(\text{CO})_5$  photoproduct allow us to determine mechanistic details of the relaxation of the excited state of this species. We find that  $\text{Cr}(\text{CO})_5$  decays to the ground state via a Jahn–Teller (symmetry-induced) conical intersection, at a trigonal bipyramid geometry. The molecule then oscillates in the well of the “moat” surrounding this conical intersection. Our results provide evidence for the dissociation mechanism proposed by Fuß et al.<sup>1–3</sup> Both the computed frequency of the coherent oscillation and the delay time until this motion is observed are in good agreement with experimental results.

## Introduction

The Fuß group have recently studied<sup>1–3</sup> the photodissociation of  $\text{Cr}(\text{CO})_6$  with femtosecond pump–probe spectroscopy. Two very fast electronic relaxation processes are observed initially. In these initial steps, Jahn–Teller relaxation occurs among the metal-to-ligand charge transfer (MLCT) states to the  $S_1$  ligand field (LF) state within 30 fs. This is followed by the loss of a CO ligand within the next 20 fs to yield  $\text{Cr}(\text{CO})_5$  in its  $S_1$  state. Subsequent electronic relaxation (internal conversion) from  $S_1$  to  $S_0$  in the photoproduct then occurs in the next ca. 40 fs and  $\text{Cr}(\text{CO})_5$  is observed on the ground state within 100 fs after photoexcitation. Fuß et al. suggest that the ultrafast nature of this photodissociation process indicates that a conical intersection is involved. However, one of the most interesting features of the Fuß experiments is the observation of coherent oscillations in the ion signals of all fragment ions. The rationalization of these data provides the stimulation for the present “on the fly” dynamics simulations reported in this work.

In the Fuß results, all fragment ions exhibit an oscillation of the same period and phase. The Fourier transform of the oscillatory part of the signal gives the frequency of the oscillation to be  $96\text{ cm}^{-1}$ . For a multidimensional potential energy surface, the vibrational energy should be partitioned in all vibrational modes and one would not expect one signal to dominate over the others. However, Fuß et al. suggest that the observed coherent oscillation is associated with the excitation of the pseudorotational coordinate in the “well” in the “moat” of the conical intersection. Our dynamics calculations will show that the excited vibration is indeed localized in the well, and it is the “circular component” that dominates. Indeed, our dynamics simulation provides detailed numerical evidence for the dissociation mechanism proposed by Fuß et al.<sup>1–3</sup>

In the condensed phase the  $\text{Cr}(\text{CO})_5$  undergoes vibrational “cooling” via energy relaxation in the condensed phase environment.<sup>4</sup> However, in the gas phase the  $\text{Cr}(\text{CO})_5$  undergoes the

sequential stripping of all remaining CO ligands to leave the bare metal atom. Fuß attributes a time constant of around 1 ps to the loss of a CO ligand from the  $\text{Cr}(\text{CO})_5$  photoproduct. Additional ligands are then stripped off after ionization i.e., all of the oscillating mass signals are produced by ionization of the  $\text{Cr}(\text{CO})_5$  photoproduct.

The potential surface suggested by the Fuß experiments, other spectroscopic results, and previous computations is illustrated schematically in Figure 1 (which has been adapted from ref 2). Initial excitation occurs to a manifold of charge transfer states ( $^1A_{1g} \rightarrow a, b^1T_{1u}$ , see Figure 2) which are split by Jahn–Teller interactions. The  $a^1T_{1u}$  state arises from the configuration  $2t_{2g}^6 \rightarrow 2t_{2g}^5 9t_{1u}^1$  while the  $b^1T_{1u}$  state arises from the configuration  $2t_{2g}^6 \rightarrow 2t_{2g}^5 2t_{2u}^1$ . These states cross, along the dissociation coordinate, to a repulsive  $^1E$  LF excited state, whose orbital configuration is shown in Figure 3 for  $O_h$  and  $C_{4v}$  symmetry. The energy of this repulsive LF state then drops steeply along the linear dissociation coordinate (in which a CO ligand is removed to infinity keeping the Cr–C–O angle fixed to  $180^\circ$ ). However, this dissociative  $^1E$  state will not be strictly degenerate due to Jahn–Teller interactions. In our calculations on  $\text{Cr}(\text{CO})_6$ , to be discussed subsequently, the two components of the  $^1E$  state are split by around  $19\text{ kcal mol}^{-1}$  after the CO ligand has been ejected.

The potential surface of  $\text{Cr}(\text{CO})_5$  in the  $S_1$  state, after the loss of the CO ligand, is shown on the right of Figure 1. The electronic structure of the  $\text{Cr}(\text{CO})_5$  corresponds to the right-hand side of Figure 3 (i.e., an  $^1E$  split by Jahn–Teller interactions) and is the same as that of the original  $\text{Cr}(\text{CO})_6$  since the CO ligand is dative bonded to the metal. At  $D_{3h}$  trigonal bipyramid (TBP) geometries, the electronic structure has the form illustrated on the left of Figure 4. The  $(e')^2$  configuration corresponds to a Jahn–Teller degeneracy which Fuß suggests corresponds to the ultrafast radiationless decay pathway. The “moat” of this Jahn–Teller degeneracy involves square planar  $C_{4v}$  structures which are minima, and  $C_{2v}$  transition structures connected along an equatorial ligand bending coor-

\* Corresponding author.

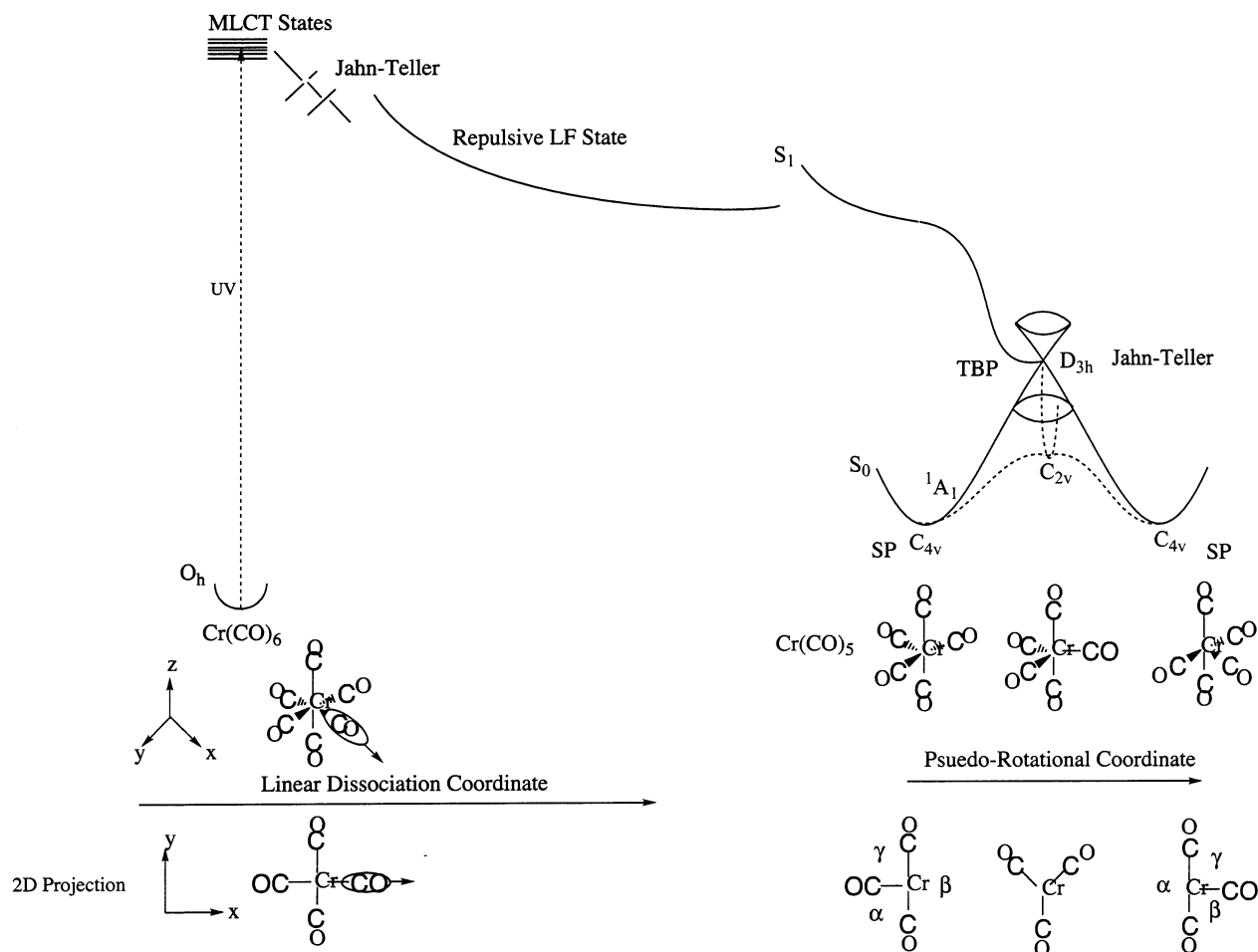


**Figure 1.** Schematic potential energy surface of linear photodissociation coordinate which leads to  $\text{Cr(CO)}_5$  in the excited state. Subsequent decay to the ground state occurs via a Jahn–Teller conical intersection with  $D_{3h}$  symmetry at TBP geometry. The molecule can then pseudo-rotate in the moat of the conical intersection. The pseudorotational coordinate is an antisymmetric bend of the three in-plane ligands.

dinate. Thus, there are three equivalent SP minima connected by transition states of  $C_{2v}$  symmetry (dashed lines in Figure 1). A path from one minimum to the next (via the transition state), to the next and back to the original minima is an example of a pseudorotational coordinate. In the case of  $\text{Cr(CO)}_5$  we will show that there is a significant computed barrier to free pseudorotation ( $10.6 \text{ kcal mol}^{-1}$ ). Fuß assigns the coherent oscillations in the ion signals of all fragment ions to motion in this moat.

Our objective in this paper is to describe the mechanism of photodissociation of  $\text{Cr(CO)}_6$  and the dynamics of the pseudo-rotation in the Jahn–Teller moat of  $\text{Cr(CO)}_5$ . “On the fly” CASSCF dynamics for a molecule of this size is rather expensive. Accordingly, we must make some approximations. These will be discussed fully in the next section. However, our CASSCF active space is limited to the description of the LF states alone. This can be justified on the basis of spectroscopic results and other more accurate computations. Thus we now briefly review these data.

The absorption spectrum of  $\text{Cr(CO)}_6$  shows two broad and intense bands<sup>5</sup> corresponding to MLCT excitations ( $^1A_{1g} \rightarrow a, b^1T_{1u}$ ). Two weak shoulders are also observed, one on the low energy side of the first MLCT band and one between the two MLCT bands. These were originally assigned as vibrational components of ligand field (LF) excited states. The low energy shoulder was assigned to the  $a^1T_{1g}$  state ( $2t_{2g}^6 \rightarrow 2t_{2g}^5 6e_g^1$ ), while the higher energy shoulder was attributed to the  $a^1T_{2g}$  state ( $2t_{2g}^6 \rightarrow 2t_{2g}^5 6e_g^1$ ) (Figure 3). Irradiation of these shoulders

leads to the ejection of a CO ligand, suggesting that the photodissociation occurs on an excited LF state. However, recent high-level theoretical studies have shown that the ligand field excited state is not populated directly. Pierloot et al.<sup>6</sup> have calculated the electronic spectra of  $\text{Cr(CO)}_6$  with CASSCF/CASPT2 and have shown that the low energy shoulder is due to a symmetry forbidden MLCT excitation and not a LF excitation. Further, Baerends et al. have also shown, using both  $\Delta\text{SCF-DFT}$ <sup>7</sup> and relativistic time-dependent density functional theory (TDDFT),<sup>8</sup> that these excitations are MLCT and not LF excitations. Thus CASSCF/CASPT2 and TDDFT show that LF states lie at much higher energy.

Baerends et al.<sup>7</sup> have shown that the MLCT states themselves are not intrinsically dissociative, but there is an avoided crossing with a steeply descending LF excited-state potential surface. As the metal–CO distance is lengthened a  $6e_g$  orbital (which is antibonding between the metal and the ligand) becomes lower in energy and rapidly becomes the lowest energy virtual orbital. By examining the descent in symmetry from  $O_h \rightarrow C_{4v}$  (Figure 3) it can be seen that the lowest LF excited states will be  $^1E$  and  $^1B_2$ . The  $^1E$  state leads to dissociation. The  $a^1E$  and  $a^1B_2$  states arise from the  $a^1T_{2u}$  and  $a^1E_u$  MLCT states upon symmetry reduction and will undergo an avoided crossing with LF states of the same symmetry along the CO dissociation path. The LF excited states arise from the configurations  $b_2^2e^4 \rightarrow b_2^2e^3a_1^1$  ( $^1E$ ) and  $b_2^2e^4 \rightarrow b_2^1e^4a_1^1$  ( $^1B_2$ ) (Figure 3).

On the basis of the above evidence, the dynamics of the photodissociation can be studied on the  $^1E$  ligand field excited

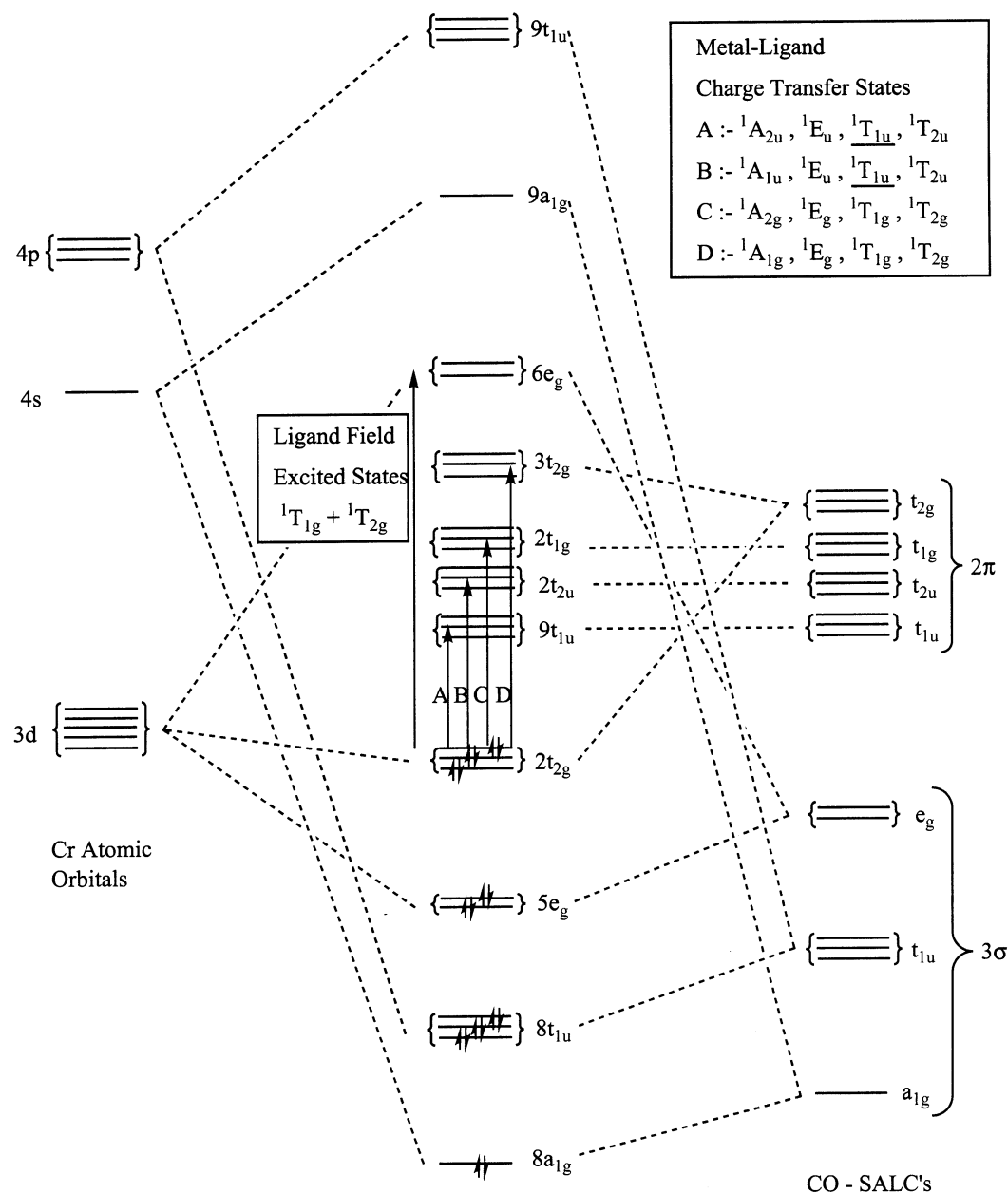


**Figure 2.** Qualitative MO diagram for  $\text{Cr}(\text{CO})_6$ . The only two orbitally and spin allowed transitions are MLCT( $d\pi^*$ )  ${}^1A_{1g} \rightarrow a^1T_{1u}$  ( $2t_{2g}^6 \rightarrow 2t_{2g}^5 2t_{2u}^1$ ) and  $b^1T_{1u}$  ( $2t_{2g}^6 \rightarrow 2t_{2g}^5 2t_{2u}^1$ ). The ligand field excited states ( ${}^1T_{1g}$  and  ${}^1T_{2g}$ ) lie higher in energy.

state. The CASSCF wave function was constructed using the lowest four d orbitals plus their antibonding counterparts. The photodissociation will be modeled on the ligand field ( $d\sigma^*$ ) excited state of the hexacarbonyl.<sup>5</sup> The driving force for photodissociation on a LF state can be rationalized using either molecular-orbital (MO) or valence-bond (VB) theories. The ligand field excited states  ${}^1T_{1g}$  and  ${}^1T_{2g}$  can be formally thought of as  $d\sigma^*$  excited states since the  $6e_g$  orbitals are antibonding between the metal d orbitals and the  $3\sigma$  orbitals of the ligand. The  $d\sigma^*$  state will be repulsive along the entire dissociation coordinate. Alternatively, the excitation can be rationalized as an electron transfer to an orbital in the same region of space as a metal–ligand  $\sigma$  bond, causing a ligand to be ejected due to electrostatic repulsion.

### Methodology and Computational Details

The potential energy surfaces of both  $\text{Cr}(\text{CO})_6$  and  $\text{Cr}(\text{CO})_5$  were studied using a complete active space self-consistent field

(CASSCF) wave function using a development version of the *Gaussian*<sup>9</sup> program. The minimum active space required to span the metal d orbitals in  $\text{Cr}(\text{CO})_5$  is CAS(6,4), where 6 electrons are allocated in the 4 lowest lying Cr 3d orbitals (see the electronic configurations shown in Figure 3 and Figure 4). The fifth d orbital is not required in the active space to correctly describe the ground and lowest excited states of  $\text{Cr}(\text{CO})_5$  ( $X^1A_1$ ,  $a^1E$ ,  $a^1B_2$  at  $C_{4v}$  symmetry). Due to the dative character of the bonds, intra-orbital electron correlation is known to be important. Thus, one needs to augment the active space with extra “antibonding” d orbitals, which have a node in the inter-nuclear (M–L) region (see Persson et al.<sup>10</sup>) to give a CAS(6,8) active space.

Because of the heavy computational demands of the direct dynamics, a modest AO basis was used (LanL2DZ basis, with the LanL2 effective core potential for chromium,<sup>11</sup> and a D95 basis on first row atoms). The standard LanL2DZ basis set does not include polarization functions (f functions on the chromium

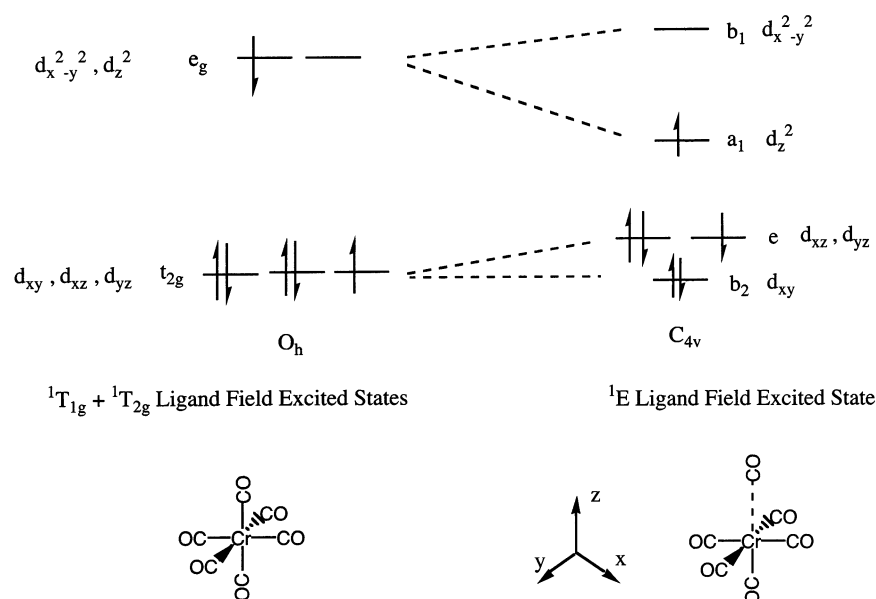


Figure 3. Orbital correlation between  $O_h$  and  $C_{4v}$  geometries.  $C_{4v}$  geometry applies to both  $\text{Cr}(\text{CO})_5$  and  $\text{Cr}(\text{CO})_6$ .

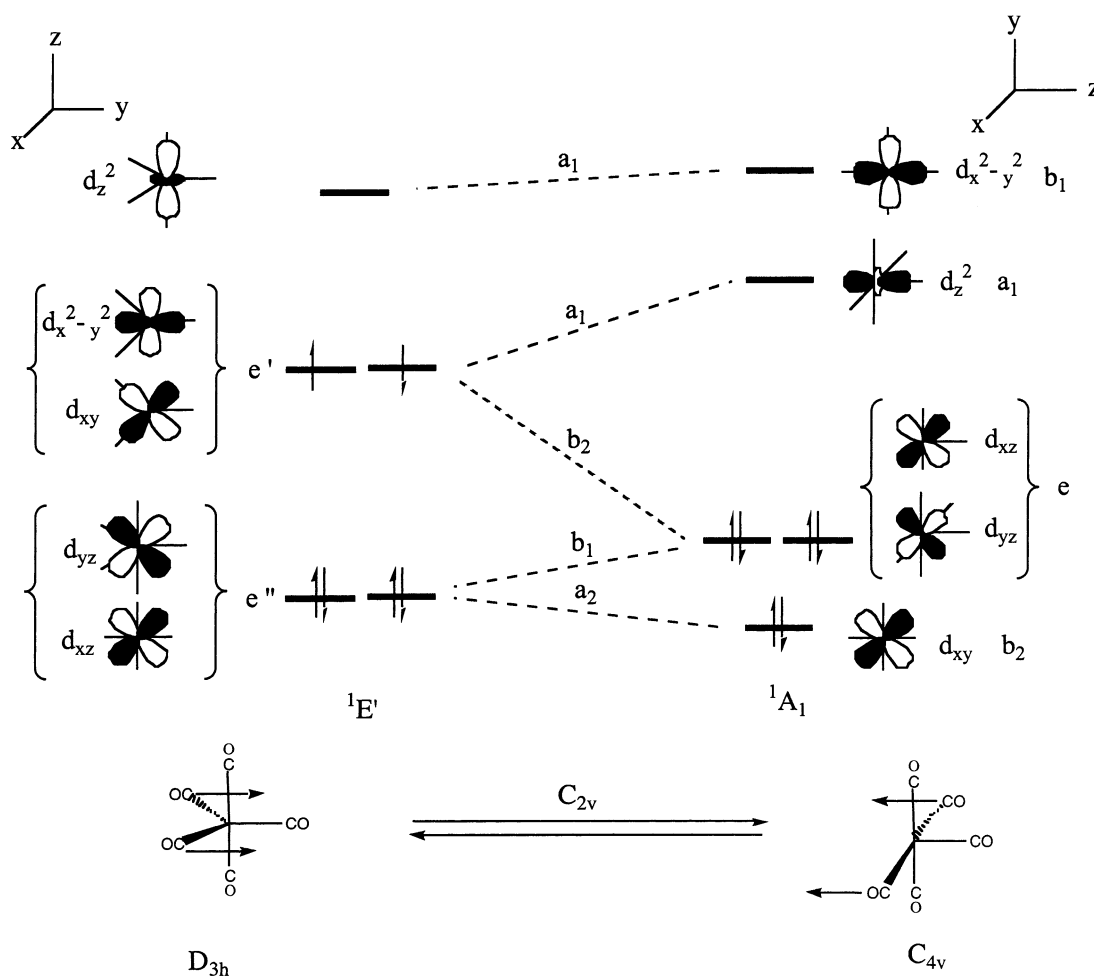


Figure 4. Orbital correlation diagram between  $D_{3h}$  (TBP) and  $C_{4v}$  (SP) geometries. TBP geometry is Jahn–Teller unstable (ground state is  ${}^1E'$ ).

and d functions on the carbon atoms and oxygen atoms). Accordingly, we investigated the importance of polarization functions by optimizing all  $\text{Cr}(\text{CO})_5$  critical points ( $C_{4v}$  minima,  $D_{3h}$  Jahn–Teller conical intersection,  $C_{2v}$  saddle points) and the dissociated  $\text{Cr}(\text{CO})_4-(\text{CO})_2$  saddle point on the  $\text{Cr}(\text{CO})_6$  potential surface (discussed later) with both the LanL2DZ basis

set and an expanded basis set which also included polarization functions as optimized for chromium<sup>12</sup> and for carbon as well as oxygen.<sup>13</sup> By examining the optimized geometries and energy differences between them, it was decided that the inclusion of polarization functions in the basis was unnecessary (see Table 1 for energetics).

TABLE 1: Cr(CO)<sub>5</sub> Energetics

optimized point	CAS(6,8)/LanL2DZ		CAS(6,8)/LanL2DZ+Pol. <sup>a</sup>		B3LYP/SDD+pol. <sup>a</sup>	
	energy (au)	energy rel. to C <sub>4v</sub> min. (kcal mol <sup>-1</sup> )	energy (au)	energy rel. to C <sub>4v</sub> min. (kcal mol <sup>-1</sup> )	energy (au)	energy rel. to C <sub>4v</sub> min. (kcal mol <sup>-1</sup> )
C <sub>4v</sub> SP min.	-649.14416	0.0	-649.47352	0.0	-653.60738	0.0
C <sub>2v</sub> TS	-649.12732	10.57	-649.45877	9.26	-653.58572	13.59
D <sub>3h</sub> Jahn–Teller CI	-649.11108	20.76	-649.43672	23.09	NA	NA

<sup>a</sup> Polarization functions taken from refs 12 and 13. <sup>b</sup> 1 kcal mol<sup>-1</sup> = 0.0433 eV.

Dynamics computations were carried out using direct methods.<sup>14</sup> The gradient and Hessian are computed “on the fly” at each point on the trajectory. The gradient and the Hessian are used to generate a local fifth-order approximation to the potential surface which allows larger step sizes to be used.<sup>15</sup>

The probability of a surface hop is determined from the solution of the time-dependent Schrödinger equation which is propagated in concert with the nuclear propagation.<sup>16</sup> The time-dependent wave function in CI space is a vector,

$$\mathbf{A}(t) = \begin{pmatrix} a_1(t) \\ \vdots \\ a_K(t) \end{pmatrix} \quad (1)$$

where  $a_K$  is a complex coefficient giving the contribution of configuration K. The probability of state  $\kappa$  is given as

$$P_\kappa(t) = \mathbf{A}^\dagger(t) \mathbf{A}(t) \quad (2)$$

The rate of change of these probabilities are used to determine a surface hop. From a practical point of view, if the time step is sufficiently small, the solution of the time-dependent Schrödinger equation can be propagated as

$$\mathbf{A}(t_n) = \exp[i\mathbf{H}(t) \tau_{n-1}] \mathbf{A}(t_{n-1}) \quad (3)$$

$$\tau_{n-1} = t_n - t_{n-1} \quad (4)$$

where  $\mathbf{H}$  is the matrix representation of the Hamiltonian in the CI eigenvector basis (see, for example, refs 17, 18).

To find a suitable point to start the Cr(CO)<sub>6</sub> dynamics, an IRD<sup>19</sup> was optimized. An IRD is an extension of the IRC concept to the general case where the initial geometry is not a transition state. One computes an initial relaxation direction (IRD), which is an  $n-1$  dimensional hyperspherical cross-section of the potential energy hypersurface. The  $n-1$  dimensional search is carried out in a space orthogonal to a vector centered at the FC point. This vector is a displacement from the FC point to a point on the S<sub>1</sub> dissociation channel and will be discussed in more detail with the dynamics results.

## Results and Discussion

**Cr(CO)<sub>6</sub> and Cr(CO)<sub>5</sub> Excited-State Potential Energy Surface Topology.** We begin with the documentation of the potential surface of Cr(CO)<sub>6</sub> and Cr(CO)<sub>5</sub> from CASSCF computations as described in the computational details section. This section has two objectives: (a) we discuss the location of a suitable starting geometry for the Cr(CO)<sub>6</sub> S<sub>1</sub> (LF) trajectory, and (b) we document the energetics and geometries of the “moat” of the Jahn–Teller degeneracy involving square planar C<sub>4v</sub> minima and C<sub>2v</sub> transition structures connected along a ligand–metal–ligand (L–M–L) bending coordinate. As dis-

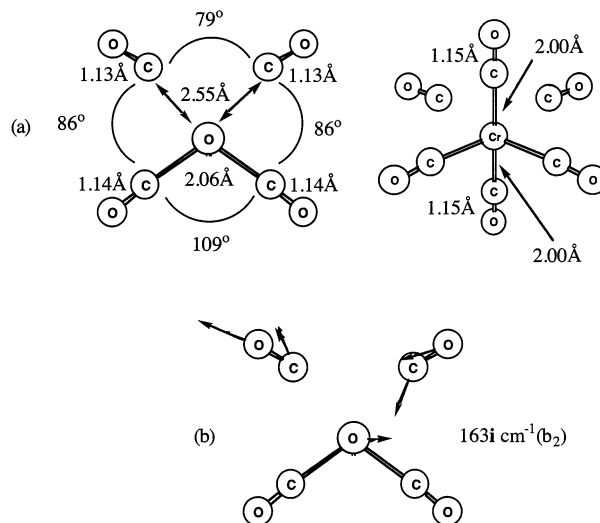


**Figure 5.** (a) CAS(6,8)/LanL2DZ optimized geometry of Cr(CO)<sub>6</sub> S<sub>1</sub> transition state with C<sub>2v</sub> symmetry. Two cis ligands are partially dissociated. (b) Transition vector—one CO dissociates leading to TBP Cr(CO)<sub>5</sub> + CO.

cussed previously, we limit our discussion in the Franck–Condon region to LF states.

We begin with our strategy for the location of a suitable starting point for the Cr(CO)<sub>6</sub> S<sub>1</sub> (LF) trajectory. Exploratory computations on the Cr(CO)<sub>6</sub> S<sub>1</sub> LF potential surface in the region close to the Franck–Condon geometry finds no intermediate minima. However, we did manage to optimize a saddle-point (geometry in Figure 5a), which connects two equivalent dissociation valleys on the Cr(CO)<sub>6</sub> S<sub>1</sub> (LF) potential surface. From Figure 5a, one can see that two cis CO ligands are partially dissociated. The transition vector (Figure 5b) corresponds to antisymmetric metal–CO bond stretching. An IRC from this S<sub>1</sub> transition state in both the forward and reverse directions leads to a trigonal bipyramidal (D<sub>3h</sub>) Cr(CO)<sub>5</sub> fragment with a dissociated CO. This IRC in effect defines last part of the CO path from the FC geometry. The problem is to document the early part of this reaction path.

Obviously, dissociation will occur along a valley on the S<sub>1</sub> potential surface. We have used the geometry at the end of the IRC to obtain a suitable starting point. The IRC leads to Cr(CO)<sub>5</sub> with trigonal bipyramid (TBP) geometry and a CO several angstroms away. An interpolation of 10 steps was then performed between this final point on the IRC and the FC point. The starting geometry was then obtained by optimizing an IRD from the FC point in this direction (see computational details).

We now turn to a documentation of the important features of the Cr(CO)<sub>5</sub> S<sub>1</sub> surface and the conical intersection pathway for radiationless decay to the S<sub>0</sub> surface. The important geometrical parameters which can be used to characterize both the S<sub>1</sub> and S<sub>0</sub> potential surface topology of Cr(CO)<sub>5</sub> are the three in-plane L–M–L angles (see the scheme at the bottom left of Figure 1 where the dissociating ligand has been circled at O<sub>h</sub> geometry). For a linear dissociation coordinate there is a



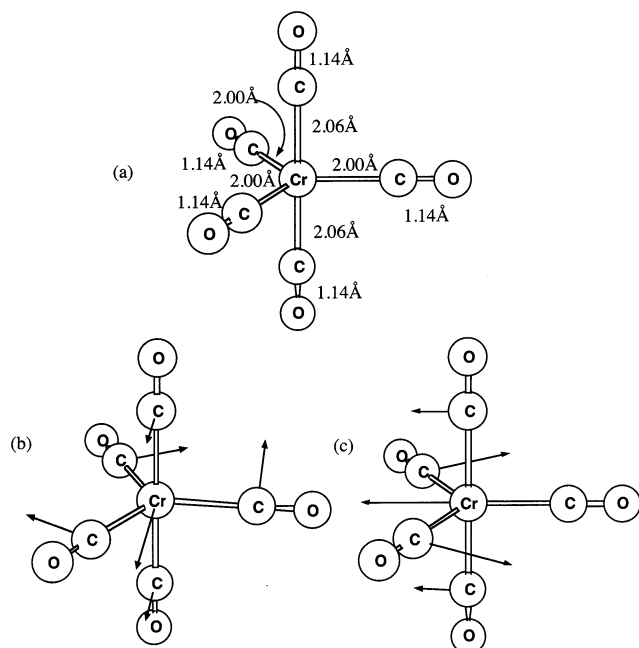


**Figure 6.** (a) Optimized conical intersection between  $S_0$  and  $S_1$  at trigonal bipyramidal geometry ( $D_{3h}$ ). (b) Derivative coupling vector (antisymmetric bending of in-plane ligands). (c) Gradient difference vector (symmetric bending of in-plane ligands). Derivative coupling and gradient difference vectors span  $e'$ .

symmetry reduction from  $O_h$  to  $C_{4v}$  (as in Figures 2 and 3). Thus, the dissociating ligand of  $\text{Cr}(\text{CO})_6$  leaves three in-plane ligands, and the ligand trans to the dissociating ligand becomes the apical ligand of the  $C_{4v}$  square pyramidal (SP)  $\text{Cr}(\text{CO})_5$ .

Once a CO ligand has been ejected, the  $\text{Cr}(\text{CO})_5$  is in its  $S_1$  state with a quasi- $C_{4v}$  SP geometry. The symmetry is broken and the geometry is not exactly  $C_{4v}$ , therefore the  $S_1$  state is one component of the  ${}^1E'$  degenerate state. At  $D_{3h}$  trigonal bipyramidal (TBP) geometries there must be a Jahn–Teller conical intersection<sup>20</sup> (see right-hand side of Figure 1) associated with the  ${}^1E'$  electronic state (see left side of Figure 4). We note that the lowest electronic state at  $D_{3h}$  symmetry is indeed the  ${}^1E'$  state. The direct product  $e' \otimes e'$  yields the following electronic states:  ${}^1E'$ ,  ${}^1A_1'$ ,  ${}^3A_2'$ . In our computations the  ${}^1E'$  state was the lowest i.e.,  $S_0$  and  $S_1$  were exactly degenerate at  $D_{3h}$  geometries.

As we shall demonstrate in our dynamics computations, this point provides the funnel for radiationless deactivation of the  $S_1$  state. The optimized geometry of the conical intersection is given in Figure 6a. The degeneracy of the electronic state is lifted by nuclear motion in the so-called “branching space”. This is the space spanned by the derivative coupling and gradient difference vectors (Figure 6b,c).

The “branching space” coordinates are the directions that lift the electronic degeneracy and define the coordinates which form the “moat” of the Jahn–Teller conical intersection. This Jahn–Teller conical intersection surface is defined in terms of depth, and possible minima and transition states and is illustrated in the subspace of “branching space” coordinates in Figure 7. The  $D_{3h}$  trigonal bipyramidal (TBP) geometry lies at the center of this figure. The “moat” around the Jahn–Teller point occurs as a result of the linear Jahn–Teller coupling between the components of the degenerate electronic state via the “branching space”.<sup>21</sup> If only linear coupling is considered, the “moat” would be completely flat (i.e., a “trough”) and the molecule could freely pseudo-rotate. When quadratic coupling is also considered, however, “bumps” develop in the moat which

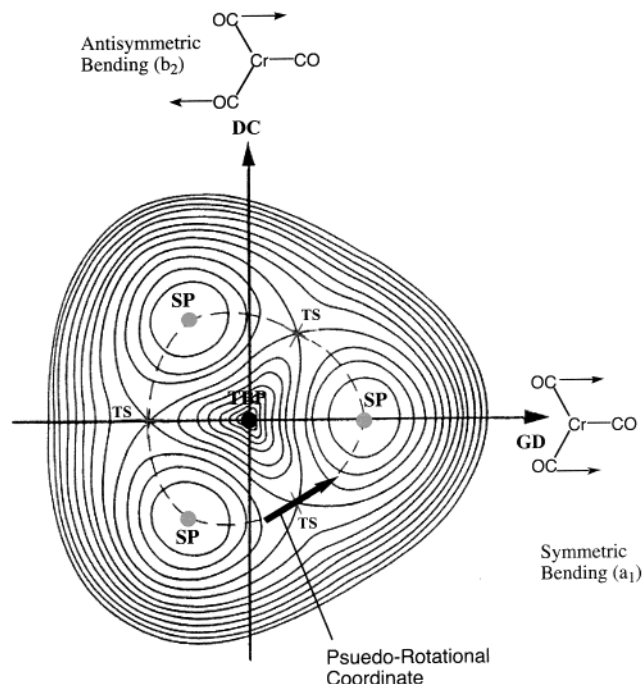


**Figure 7.** Moat around TBP ( $D_{3h}$ ) Jahn–Teller conical intersection. The “branching space” coordinates are the gradient difference and derivative coupling vectors. These correspond to symmetric and antisymmetric bending, respectively.

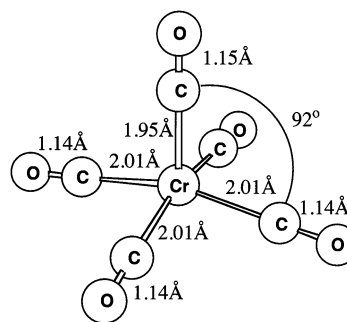


**Figure 8.** Square pyramidal (SP) minimum energy geometry optimized with CAS(6,8)/LanL2DZ.

correspond to transition states (TS) between the various equivalent (localized) minima. This has the consequence that there is a barrier to pseudorotation. This also allows an alternative definition of the pseudorotational coordinate as the transition vector at one of the equivalent transition states.

There are three equivalent minima (obtained by exchanging apical and basal ligands as shown in bottom right of Figure 1), with square pyramidal (SP) geometries and  $C_{4v}$  symmetry, in the “moat” surrounding the TBP Jahn–Teller point. The optimized structure is shown in Figure 8. The transition states have  $C_{2v}$  symmetry and the optimized geometry is shown in Figure 9.

The barrier (between SP minima and the transition states in the moat), calculated with CASSCF, is 10.6 kcal mol<sup>-1</sup>. This computation neglects dynamic electron correlation. Accordingly, we recalculated the barrier height using density functional theory (B3LYP functional) and using the Stuttgart/Dresden effective core potential<sup>22</sup> basis set with polarization functions added to the carbon and oxygen atoms.<sup>13</sup> DFT is suitable to calculate the barrier height as both the  $C_{4v}$  SP minima and  $C_{2v}$  transition states are closed shell species (see Figure 4). The calculated barrier height at this level of theory is 13.6 kcal mol<sup>-1</sup>. Thus,

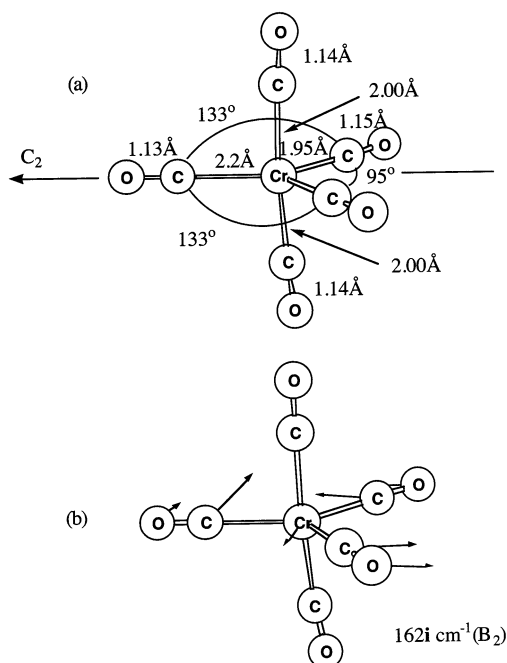


**Figure 9.** (a) CAS(6,8)/LanL2DZ optimized geometry of  $S_0$   $\text{Cr(CO)}_5$   $C_{2v}$  transition state. (b) Transition vector which defines the pseudorotational coordinate.

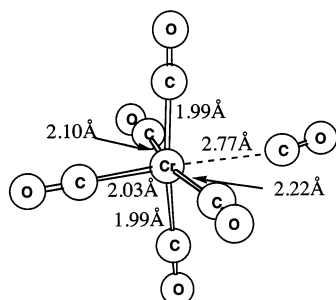


**Figure 10.** Geometry used to start dynamics calculations on  $\text{Cr(CO)}_6$   $S_1$  state. Obtained as an IRD optimized between the FC point ( $O_h$ ) and an interpolated point from  $S_1$  IRC.

CASSCF computations should be adequate to describe the dynamics of motion in the moat.

**$\text{Cr(CO)}_5$  and  $\text{Cr(CO)}_6$  Dynamics.** Our objective is to generate a “model” trajectory which describes the dynamics in the Jahn–Teller conical intersection moat. The starting conditions for such a dynamics computation is the geometry and momenta of the  $\text{Cr(CO)}_5$  fragment after dissociation of  $\text{Cr(CO)}_6$ . Accordingly, the photodissociation of  $\text{Cr(CO)}_6$  was studied in order to simulate suitable starting conditions for the subsequent  $\text{Cr(CO)}_5$  dynamics study.

The starting conditions for this model  $\text{Cr(CO)}_6$  photodissociation need some discussion. As discussed previously, due to the computational cost of dynamics calculations we can run only a representative trajectory for the  $\text{Cr(CO)}_6$  dissociation. As discussed in the computational details section, we have started this trajectory with no initial momenta (i.e., no energy given to any vibrational modes) at an optimized point on the  $\text{Cr(CO)}_6$  dissociation valley, slightly displaced from the FC region. This geometry is shown in Figure 10, where one can see that the major deviation from an  $O_h$  geometry is that one of the metal–ligand bond lengths is elongated with respect to the others. Thus, in our dynamics we neglect any effects resulting from the decay from the MLCT states in the Franck–Condon region. We also assume that this point is at the “center” of the distribution that

might be obtained by sampling the ground-state vibrational modes at the octahedral minimum.

Snapshots of the model  $\text{Cr(CO)}_6$  dissociation trajectory are given in Figure 11. The CO ligand can be seen to leave rapidly. The dissociation coordinate is dominated by the metal–ligand distance of the dissociating CO. Dissociation is complete within 100 fs, and the CO ligand is rotationally excited as it leaves. The fact that the CO is rotationally excited supports experimental evidence that the rotational temperature of the ejected CO is found to be hotter than room temperature for a group VI metal carbonyl.<sup>23</sup> The observed higher rotational CO temperatures for other transition metal carbonyls ( $\text{Fe(CO)}_5$ <sup>24</sup> and  $\text{Ni(CO)}_4$ <sup>25</sup>) is probably due to a similar mechanism.

A small amount of vibrational energy “leaks” into other modes along the dissociation coordinate. This vibrational excitation has important consequences in the initial conditions of the dynamics of  $\text{Cr(CO)}_5$ . Thus, after several femtoseconds, a symmetric bending vibration of two trans CO ligands which are both cis to the ejected ligand (Figure 11) becomes excited (see the angle changes indicated in Figure 11) and the value of the apical-basal ligand angle increases by  $12^\circ$  during the duration of the  $\text{Cr(CO)}_6$  trajectory. Essentially the two ligands “collapse” in order to fill the coordination “hole” left by the ejected CO ligand. Vibrational energy redistribution from the antisymmetric stretch to the symmetric bend occurs along the dissociation coordinate. Anharmonicity of the potential surface will cause these modes to mix and allow energy to “leak” from one mode to the other.

We now discuss the dynamics of the  $\text{Cr(CO)}_5$  species. We begin with the initial conditions determined from the preceding  $\text{Cr(CO)}_6$  trajectory. As we have just discussed, the bending mode seen in the  $\text{Cr(CO)}_6$  trajectory becomes the dominant nuclear motion once the CO ligand has left. Due to the mass of the chromium atom, the center of mass in both the dissociated  $\text{Cr(CO)}_5$ –CO and the  $\text{Cr(CO)}_5$  fragment are essentially the same. Therefore the effect of the changing the center of mass on the position and momenta vectors of the remaining  $\text{Cr(CO)}_5$  is negligible.

The  $\text{Cr(CO)}_5$  photoproduct has a quasi-square pyramidal geometry (see initial geometry of Figure 12). The symmetry is sufficiently broken, however, that the first excited state is not degenerate (compare with the idealized linear dissociation coordinate of Figure 5). There is an energy gap of  $19 \text{ kcal mol}^{-1}$  between  $S_1$  and  $S_2$  at the starting geometry for the  $\text{Cr(CO)}_5$  trajectory (calculated by means of a CI calculation). This means that the entire excited state dynamics can be studied by considering only the  $S_1$  state and its coupling to the ground state.

The results of our model trajectory of  $\text{Cr(CO)}_5$  started using the geometries and momenta obtained from the  $\text{Cr(CO)}_6$  photodissociation trajectory are summarized in Figures 12–16. Figure 12 contains geometric information with “snapshots” of the molecular geometry at various times. Figure 13 gives the information that is obtained from the propagation of the time-dependent electronic wave function. This information is used to determine the surface hops. Figure 14 shows a schematic representation of the trajectory in the “branching space” of the conical intersection. Figure 15 shows the gradients at the surface hop down and we return to this subsequently. Finally, Figure 16 shows the changes in the L–M–L angles associated with motion in the Jahn–Teller “moat”. It should be noted that Figure 16 contains data for both the  $\text{Cr(CO)}_6$  and  $\text{Cr(CO)}_5$  trajectories.

To assimilate and interpret our nonadiabatic (i.e., two coupled surfaces are involved, ground and excited state) dynamics it is

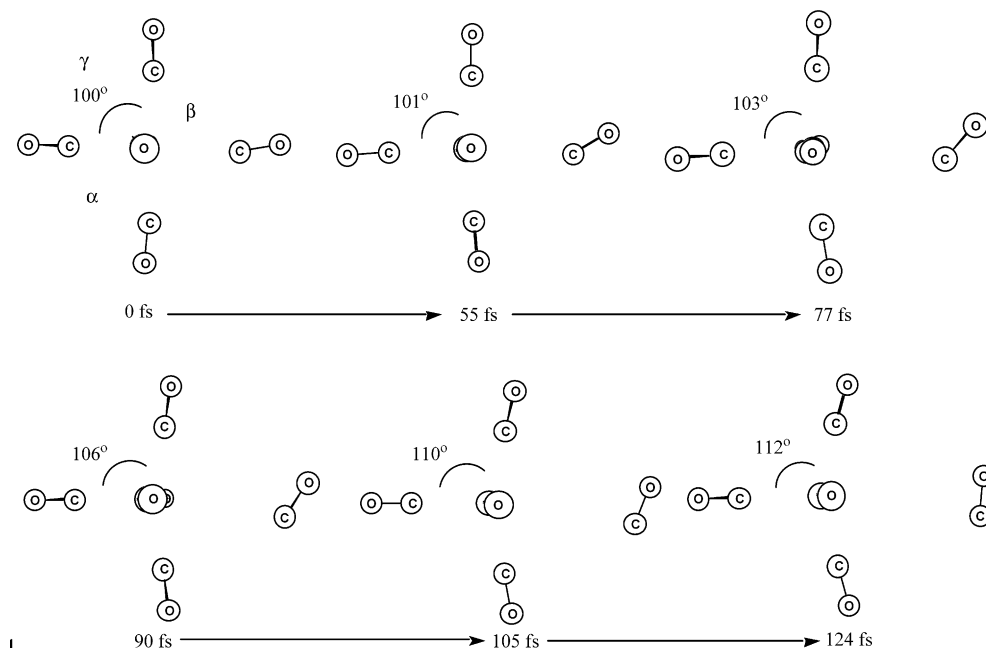


**Figure 11.** Snapshots along  $\text{Cr}(\text{CO})_6$  trajectory. The CO leaves in rotationally excited state and the large amplitude symmetric bending motion becomes excited.

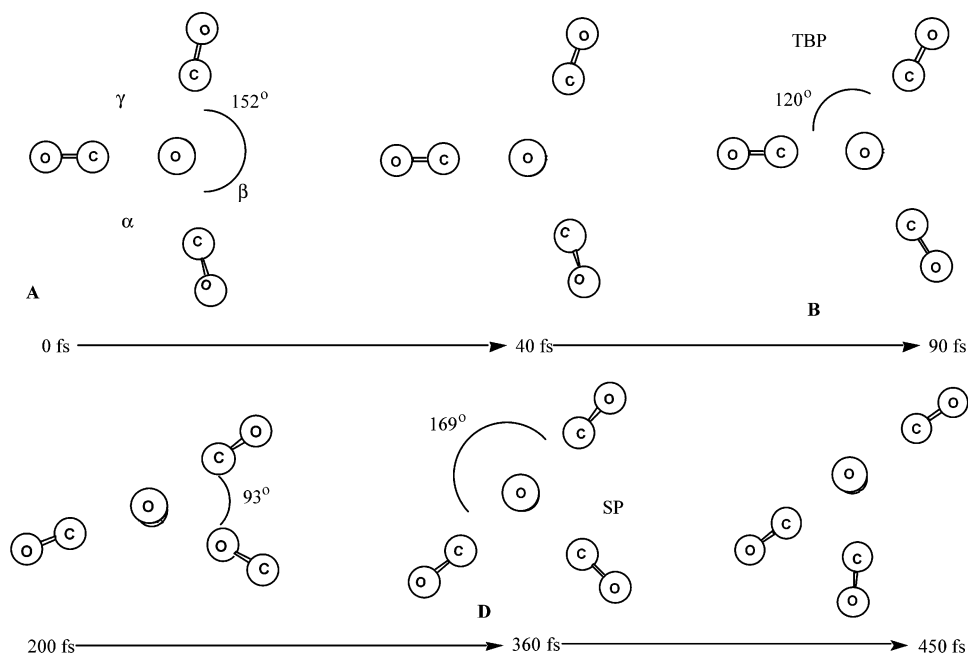


**Figure 12.** Snapshots along the  $\text{Cr}(\text{CO})_5$  trajectory.

essential to appreciate that the motion through the surface crossing regions is essentially diabatic. Thus, the transition from the upper part of the conical intersection to the lower part occurs with no discontinuities in the gradients and the surface hops are instantaneous (see the sharp transitions in Figure 13). On examination of Figure 13, one can observe that the system decays to the ground state in 90 fs, returns to the excited state after a partial vibration on the ground state, and then returns to the ground state again after 30 fs. However, remarkably, the force field felt by the nuclei is not really affected by the nonadiabatic event and geometrical motion is dominated by simple motion in the branching space: the L–M–L coordinates of the Jahn–Teller “moat” shown in Figure 14. The trajectory behaves as if a single quasi-adiabatic potential surface was involved. This point is important because it explains why one

can see coherent oscillations in the spectroscopic measurements that are associated with motion in these coordinates. Thus, we can focus our attention on the geometrical and energetic changes along the trajectory and we can ignore the fact that motion takes place on two surfaces with the intervention of several non-adiabatic events. Finally we should also point out that our recrossings are not an artifact of the use of an insufficient number of nuclear degrees of freedom (see the  $S_2 \rightarrow S_1$  decay in pyrazine<sup>26</sup>). All nuclear degrees of freedom are included in the trajectory

We now discuss the geometrical changes that occur along the  $\text{Cr}(\text{CO})_5$  trajectory using Figure 12 (snapshots of the geometry), Figure 14 (motion on a schematic representation of the  $S_0$  ground-state potential surface), and Figure 16 (changes in the L–M–L angles along the trajectory). The dynamics has



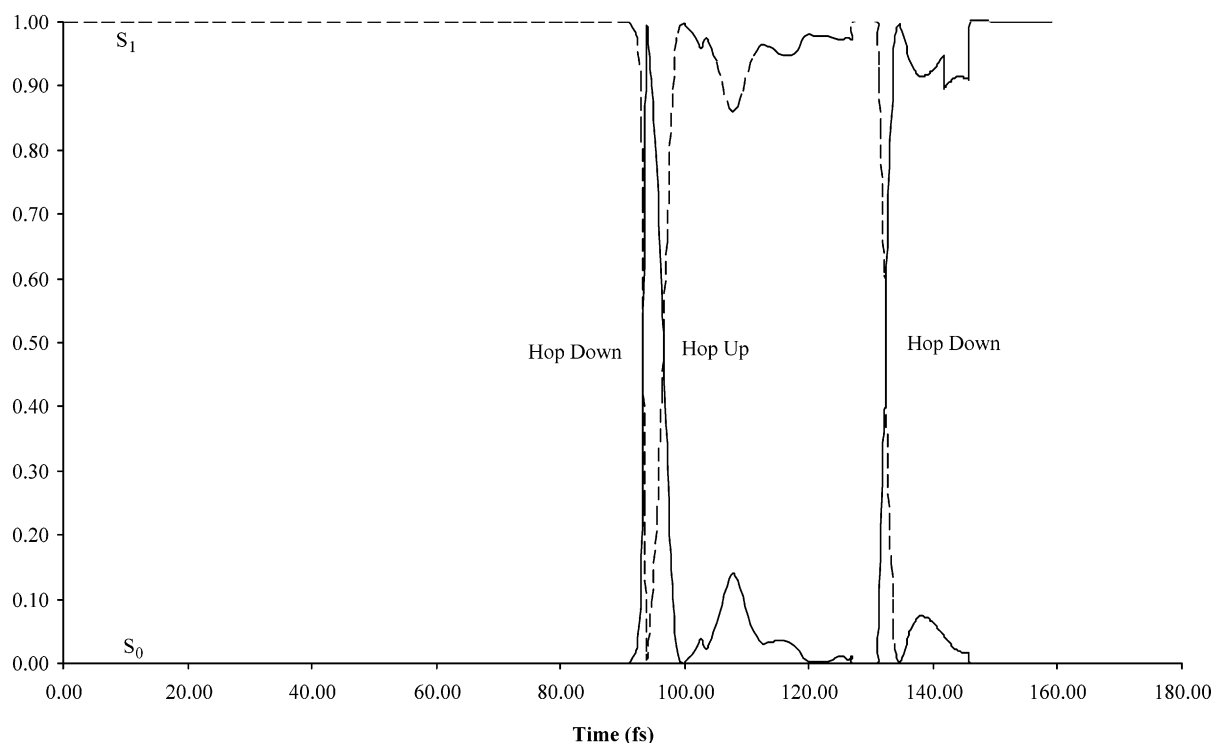


**Figure 13.** Amplitudes of states  $S_0$  and  $S_1$  in the time-dependent wave function computed along the trajectory in the degenerate region. There is a diabatic hop after 90 fs followed by recrossing within 5 fs. After a further 30 fs there occurs another diabatic hop down and the molecule then remains on the ground-state surface.

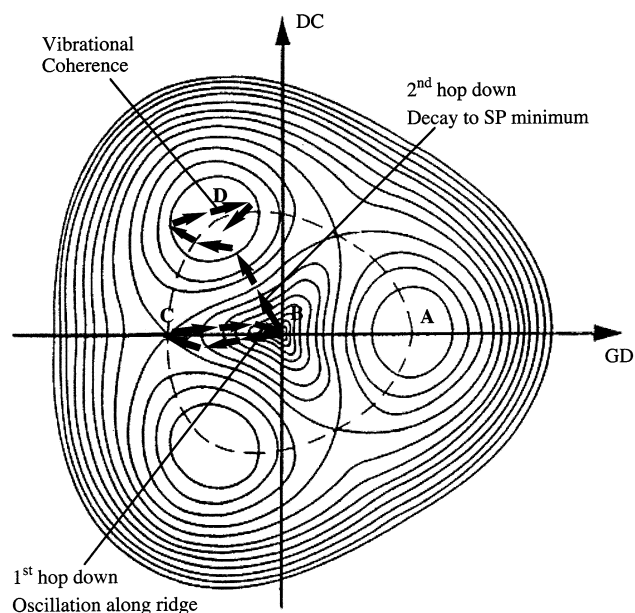


**Figure 14.** Representation of the  $\text{Cr}(\text{CO})_5$  trajectory on the ground-state surface. There is an oscillation along the ridge before recrossing to the upper surface, followed by the final decay to the ground state where the molecule becomes trapped in a SP minimum well, leading to the observed vibrational coherence.

three distinct phases, and the ground-state motion is shown schematically in Figure 14. The first phase involves motion in the radial coordinate of the Jahn–Teller surface (symmetric bend, phase 1 in Figure 16). The excited state decays from the geometry **A** (Figure 14) via the conical intersection **B**, followed by a partial oscillation on the ridge of the transition state region **C**. The second phase involves the “leakage” of energy into the antisymmetric bending or pseudorotational coordinate. The transfer of energy takes place along the partial vibration along

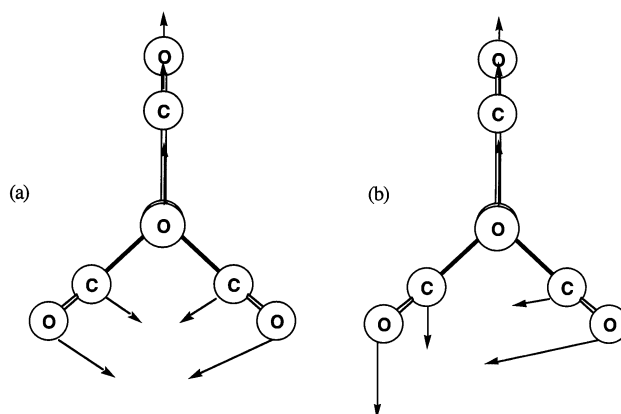


**Figure 15.** (a) Momenta vector prior to the first diabatic hop down (symmetric). This vector is parallel to the gradient difference vector. (b) Momenta vector prior to the second diabatic hop down (antisymmetric).

the transition state ridge and during the subsequent excursion back onto the excited state before returning to the ground state along a mixture of symmetric and antisymmetric bends. Finally, the third phase involves motion trapped in the well of the surface near point **D** that corresponds to the coherent oscillations observed by Fuß. We now give a more detailed discussion of these three phases.

In the first phase of the dynamics, the trajectory starts at a square pyramidal geometry (i.e., the geometry corresponds to point **A** in Figure 14 but the trajectory is on the upper branch,  $S_1$ , and so is not shown in the figure). The initial momenta are derived from the  $\text{Cr}(\text{CO})_6$  trajectory, and motion is dominated by the apical-basal ligand bending. Thus the initial motion (0–90 fs in Figure 12 and shown as phase 1 in Figure 16) involves the collapse of two ligands to completely fill the coordination “hole”. The trajectory progresses toward the trigonal bipyramidal geometry with  $D_{3h}$  symmetry (point **B** in Figure 12, Figure 14,

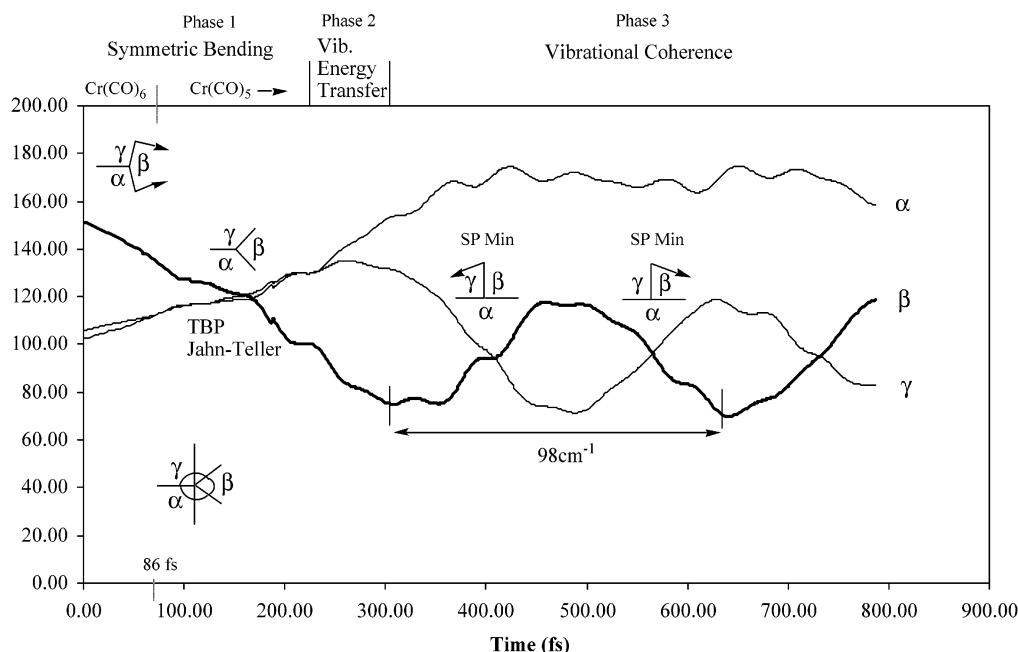


**Figure 16.** Variation in the three in-plane L–M–L angles along the entire ( $\text{Cr(CO)}_6$  and  $\text{Cr(CO)}_5$ ) trajectory. In the first phase a symmetric bend is excited and the angles  $\alpha$  and  $\gamma$  are seen to increase. The second phase corresponds to vibrational energy transfer from the symmetric to the antisymmetric bending coordinate. In the final phase the molecule oscillates in a square planar minimum energy well with a frequency of  $98\text{ cm}^{-1}$ .

and indicated as the Jahn–Teller point in Figure 16). At  $D_{3h}$  geometries,  $\text{Cr(CO)}_5$  is Jahn–Teller degenerate ( $^1E'$ , see left-hand side of Figure 4). The excited symmetric bending (which is parallel to the gradient difference vector, see Figure 6c) vibration thus “funnels” the molecule toward the Jahn–Teller conical intersection (Figure 6a). Thus, the TBP geometry is reached within 90 fs (point B, Figures 12,14). At this point a diabatic surface hop occurs and the molecule decays to the  $S_0$  surface (Figure 13). As we have noted previously, there is an instantaneous population transfer at this point (Figure 13). The diabatic nature of the transition manifests itself in the fact that the direction of the momenta vector (symmetric bending shown in Figure 15a) is unchanged by the nonadiabatic event. The momenta vector at the second hop down (Figure 15b) is different, however. Antisymmetric (as well as symmetric) bending has been induced. This is due to the vibrational energy transfer in the second phase of the trajectory as we now discuss.

The second phase of the dynamics is associated with vibrational energy transfer and is illustrated in Figure 16 where the changes in the three L–M–L angles can be seen. During the second phase, the vibration changes from a symmetric to an antisymmetric bend. The angles  $\gamma$  and  $\alpha$  now no longer change in concert,  $\alpha$  tends toward  $180^\circ$ , while  $\gamma$  decreases during this phase. After the decay to  $S_0$ , the molecule remains on the  $S_0$  surface for 5 fs, and undergoes a partial oscillation along the ridge of the  $C_{2v}$  saddle-point (point C Figure 14), before recrossing to the upper surface (Figure 13) near the TBP conical intersection. This partial oscillation on the ridge, marks the beginning of the second phase of the trajectory where energy gets transferred into the antisymmetric bending (or pseudorotational mode). As the system completes the second part of the oscillation, toward the TBP geometry, the molecule has started to fall off of the ridge. The antisymmetric bending mode, in addition to the symmetric bending mode, gets excited during this second phase of the trajectory.

Thus, the energy transfer in this second phase of the trajectory, gives some credence to the suggestion by Fuß et al.<sup>2</sup> that the molecule will decay to the ground-state surface along the ridge. The resonance that Fuß et al.<sup>2</sup> assign to pseudorotation is not

seen immediately after the surface crossing, but rather is delayed by a large fraction of the period of pseudorotation. This is consistent with the fact that the molecule oscillates along a radial coordinate before the wave packet is redirected toward the minimum. The second phase of the dynamics, following the partial oscillation on the ridge of the transition state, continues after recrossing onto the upper electronic state where the molecule remains for 30 fs before decaying diabatically to the ground state (Figure 13).

The third phase of the trajectory corresponds to the vibrational coherence observed by Fuß et al.<sup>1–3</sup> The right-hand side of Figure 16 shows that the angles labeled  $\beta$  and  $\gamma$  oscillate out of phase with each other but with the same period. The other angle ( $\alpha$ ) stays constant at around  $180^\circ$ . This type of vibration can be formally thought of as an apical-basal bending vibration. When the angles  $\beta$  and  $\gamma$  are equal (i.e.,  $90^\circ$ ) the molecule is at the square planar minimum. In Figure 16, the phase of the vibration at the SP minima is indicated with an arrow. The extremal values of the angles  $\beta$  and  $\gamma$  (out of phase with each other) in the third phase of the trajectory are when the molecule is close to one of the  $C_{2v}$  transition structures at either side of the minimum. In this way, the bending vibration which is excited is along the pseudorotational coordinate but the oscillation is trapped in the minimum energy well. The computed frequency of the oscillation is  $98\text{ cm}^{-1}$ , while that observed by Fuß et al.<sup>1–3</sup> is  $96\text{ cm}^{-1}$ . Fuß experimental conditions mean that he observes only the radial component of the moat oscillation seen in our dynamics (which is a mixture of both the radial and circular motions). However, the symmetric and asymmetric bend frequencies computed at the well minimum are almost identical ( $84$  and  $104\text{ cm}^{-1}$ ).

The results of our “model” trajectory compare favorably with the experimental data of Fuß. Qualitatively, we both observe that a CO ligand is lost on an ultrafast time scale (less than 100 fs). Fuß assigns a time of 53 fs until the dissociation is complete. In our trajectory we assume that the CO ligand has dissociated when the metal–ligand bond distance is greater than the sum of the chromium and carbon van der Waals radii ( $3.7\text{ Å}$ ), which occurs after 86 fs. These values are in reasonable agreement

and support the argument that the dissociation occurs on a steep ligand-field excited-state potential surface.

While we are unable to compare the three distinct phases observed in our trajectory with the steps in Fuß's mechanism, we are able to compare the total time taken from excitation until the first maximum of the coherent oscillation is observed. Fuß observes a delay of around 400 fs until the first maximum of coherent oscillation and our trajectory are in good agreement. In Figure 16, the three in-plane L–M–L angles are shown for the entire "reaction" trajectory (i.e., for the Cr(CO)<sub>6</sub> and Cr(CO)<sub>5</sub> trajectories combined). The first maximum of coherent oscillations occurs when the angles  $\beta$  and  $\gamma$  are both equal to 90° (for circular motion). This occurs around 400 fs. However, as pointed out above, only the radial component is observed experimentally, and in this case, the first maximum will occur around 300 fs in Figure 16. The delay time observed experimentally is somewhat dependent upon the pump wavelength so there is also reasonable agreement for the radial motion, so we have good qualitative agreement. We are thus confident that our "model" trajectory yields insight into the mechanistic features of Cr(CO)<sub>6</sub> photodissociation which are in good agreement with the time-resolved experiments of Fuß et al.<sup>1–3</sup>

## Conclusions

The dynamics of Cr(CO)<sub>6</sub> photodissociation has been studied using direct dynamics including trajectory surface hopping. Our results show three distinct phases: (1) dissociation of a CO ligand in less than 100 fs, (2) vibrational energy redistribution between the symmetric and antisymmetric bending modes, and (3) oscillation in a well around the "moat" of a Jahn–Teller conical intersection.

Our results agree very favorably with the time-resolved work of Fuß et al.<sup>1–3</sup> We compute that dissociation occurs after around 86 fs compared to 53 fs observed by Fuß. The total time from excitation until the first maximum of coherent oscillations is computed to be around 400 fs (circular motion)/300 fs (radial motion) in good agreement with experiment. Finally, we can assign the coherent oscillation observed by Fuß, as a trapped pseudorotation in the well of the "moat" surrounding the Jahn–Teller point. Our computed frequency of 98 cm<sup>−1</sup> is in agreement with that obtained by Fuß et al., and thus our dynamics simulations can provide a mechanistic explanation for the observed coherent oscillations. These are excited due to the fact the wave packet passes through a Jahn–Teller conical intersection which channels the vibrational energy into these modes.

**Acknowledgment.** All computations were carried out on an IBM-SP2 funded jointly by IBM-UK and HEFCE (UK). Financial support for this project was provided by EPSRC (UK) under Grant 98312744.

**Supporting Information Available:** The following Supporting Information is available: Cartesian coordinates of all optimized geometries, Cartesian coordinates of the starting point

of the Cr(CO)<sub>6</sub> trajectory, initial conditions for Cr(CO)<sub>5</sub> trajectory, and two quicktime movie files of the Cr(CO)<sub>6</sub> and Cr(CO)<sub>5</sub> trajectories. This material is available free of charge via the Internet at <http://pubs.acs.org>.

## References and Notes

- (1) Trushin, S. A.; Fuß, W.; Schmid, W. E.; Kompa, K. L. *J. Phys. Chem.* **1998**, *102*, 4129–4137.
- (2) Trushin, S. A.; Fuß, W.; Schmid, W. E. *Chem. Phys.* **2000**, *259*, 313–330.
- (3) Fuß, W.; Trushin, S. A.; Schmid, W. E. *Res. Chem. Intermed.* **2001**, *27*, 447–457.
- (4) Lian, T.; Bromberg, S. E.; Asplund, M. C.; Yang, H.; Harris, C. B. *J. Phys. Chem.* **1996**, *100*, 11994–12001.
- (5) Beach, N. A.; Gray, H. B. *J. Am. Chem. Soc.* **1968**, *90*, 5713.
- (6) Pierloot, K.; Tsokos, E.; Vanquickenborne, L. G. *J. Phys. Chem.* **1996**, *100*, 16545–16550.
- (7) Pollak, C.; Rosa, A.; Baerends, E. J. *J. Am. Chem. Soc.* **1997**, *119*, 7324–7329.
- (8) Rosa, A.; Baerends, E. J.; van Gisbergen, S. J. A.; van Lenthe, E.; Groenvel, J. A.; Snijders, J. G. *J. Am. Chem. Soc.* **1999**, *121*, 10356–10365.
- (9) Frisch, M. J.; Trucks, G. W.; Schlegel, H. B.; Scuseria, G. E.; Robb, M. A.; Cheeseman, J. R.; Zakrzewski, V. G.; Montgomery, J. A. A. D.; Stratmann, R. E.; Burant, J. C.; Dapprich, S.; Millam, J. M.; Daniels, A. D.; Kudin, K. N.; Strain, M. C.; Farkas, O.; Tomasi, J.; Barone, V.; Cossi, M.; Cammi, R.; Mennucci, B.; Pomelli, C.; Adamo, C.; Clifford, S.; Ochterski, J.; Petersson, G. A.; Ayala, P. Y.; Cui, Q.; Morokuma, K.; Malick, D. K.; Rabuck, A. D.; Raghavachari, K.; Foresman, J. B.; Cioslowski, J.; Ortiz, J. V.; Stefanov, B. B.; Liu, G.; Liashenko, A.; Piskorz, P.; Komaromi, I.; Gomperts, R.; Martin, R. L.; Fox, D. J.; Keith, T.; Al-Laham, M. A.; Peng, C. Y.; Nanayakkara, A.; Gonzalez, C.; Challacombe, M.; Gill, P. M. W.; Johnson, B. G.; Chen, W.; Wong, M. W.; Andres, J. L. M.; Head-Gordon, M.; Replogle, E. S.; Pople, J. A. *Gaussian 98* (Revision C.1); Gaussian, Inc.: Pittsburgh, PA, 1998.
- (10) Persson, B. J.; Roos, B. O.; Pierloot, K. *J. Chem. Phys.* **1994**, *101* (8), 6810–6821.
- (11) Hay, P. J.; Wadt, W. R. *J. Chem. Phys.* **1985**, *82*, 270–283.
- (12) Ehlers, A. W.; Bohme, M.; Dapprich, S.; Gobbi, A.; Hollwarth, A.; Jonas, V.; Kohler, K. F.; Stegman, R.; Veldkamp, A.; Frenking, G. *Chem. Phys. Lett.* **1993**, *208*, 111–114.
- (13) Dunning, T. H., Jr.; Hay, P. J. In *Modern Theoretical Chemistry*, Vol. 3; Methods of Electronic Structure Theory; Schaefer, H. F., III, Ed.; Plenum Press: New York, 1977; p 1.
- (14) Helgaker, T.; Uggerud, E.; Jensen, H. J. A. *Chem. Phys. Lett.* **1990**, *173*, 145–150.
- (15) Millam, J. M.; Bakken, V.; Chen, W.; Hase, W. L.; Schlegel, H. B. *J. Chem. Phys.* **1999**, *111*, 3800–3805.
- (16) Klein, S.; Bearpark, M. J.; Smith, B. R.; Robb, M. A.; Olivucci, M.; Bernardi, F. *Chem. Phys. Lett.* **1998**, *292*, 259–266.
- (17) Park, T. J.; Light, J. J. *J. Chem. Phys.* **1986**, *85*, 5870.
- (18) Manthe, U.; Köppel, H.; Cederbaum, L. S. *J. Chem. Phys.* **1991**, *95*, 1708.
- (19) Celani, P.; Robb, M. A.; Garavelli, M.; Bernardi, F.; Olivucci, M. *Chem. Phys. Lett.* **1995**, *243*, 1–8.
- (20) Jahn, H. A.; Teller, E. *Proc. R. Soc.* **1937**, *161*, 220.
- (21) Barckholtz, T. A.; Miller, T. A. *J. Phys. Chem. A* **1999**, *103*, 2321–2336.
- (22) Fuentealba, P.; Preuss, H.; Stoll, H.; Szentpaly, L. V. *Chem. Phys. Lett.* **1989**, *89*, 418.
- (23) Holland, J. P.; Rosenfeld, R. N. *J. Chem. Phys.* **1988**, *89*, 7217–7225.
- (24) Venkataram, B. K.; Bandukwalla, G.; Zhuangjian, Z.; Vernon, M. J. *J. Chem. Phys.* **1989**, *90*, 5510–5526.
- (25) Schlenker, F. J.; Bouchard, F.; Waller, I. M.; Hepburn, J. W. *J. Chem. Phys.* **1990**, *93*, 7110–7118.
- (26) Worth, G. A.; Meyer, H.-D.; Cederbaum, L. S. *J. Chem. Phys.* **1998**, *109*, 3518–3529.